Supplementary Material:
Size-specific transport of colloidal particles using magnetic fields

Sebastian Wohlrab,[1] Lara Schelter,[1] Aneena Rinu Perayil,[1] Piotr Kuświk,[2] Maciej Urbaniak,[2] Feliks Stobiecki,[2] Arne J. Vereijken,[3] Arno Ehresmann,[3] Thomas M. Fischer,[1] and Daniel de las Heras[4, 1, *]
[1]*Physikalisches Institut, Universität Bayreuth, D-95440 Bayreuth, Germany*
[2]*Institute of Molecular Physics, Polish Academy of Sciences, 60-179 Poznań, Poland*
[3]*Institute of Physics and Center for Interdisciplinary Nanostructure Science and Technology (CINSaT), Universität Kassel, D-34132 Kassel, Germany*
[4]*Institute for Theoretical Physics, University of Tübingen, D-72076 Tübingen, Germany*
(Dated: April 13, 2026)

A. Experimental details

The magnetic films are thin Co/Au multilayers with perpendicular magnetic anisotropy lithographically patterned via keV-He-ion bombardment [1]. For details regarding the fabrication process see references [2–4]. The length of the lattice vectors is 18 µm and the thickness of the pattern is a few nanometers. The pattern is coated with a photo-resist film of thickness 1.5 µm. The coating protects the pattern and serves as a spacer ensuring that the magnitude of the external field is larger than that of the field of the pattern, which simplifies the form of the magnetic potential (see below).

The magnetic beads used in this study are Dynabeads superparamagnetic core-shell particles (diameters 2.8 µm and 4.5 µm) with a polystyrene shell and a core consisting of polymer microspheres containing superparamagnetic iron-oxide nanoparticles. The small beads are functionalized with carboxylate, while the large beads are tosylated. The beads are immersed into deionized water on top of the pattern.

The magnitude of the external magnetic field must exceed that of the pattern magnetic field at the elevation where the colloids reside in order to approximate the magnetic potential by the dot product of the external and pattern fields, see Eq. (S3). At the same time, the external field must remain smaller than the coercive field of the thin magnetic film. Within this broad parameter range, the particle transport is independent of the strength of the external magnetic field. In the experiments, the magnitude of the uniform external field is approximately 4×10^3 A/m.

As the number of fences increases and the control loops approach these fences, the orientation of the magnetic field must be steered with increasing precision in order to remain on the desired side of the fence. In the experiments, the fences should be regarded as slightly blurred regions rather than perfectly sharp curves. The orientation of the external magnetic field can be controlled with a precision that exceeds the width of these blurred regions. In practice, we can reliably navigate between fences provided that they remain separated by an angular distance of approximately 5 degrees.

For further details regarding the experimental setup, we refer the reader to Ref. [4].

B. Magnetic potential

The magnetic colloidal particles are immersed in a solvent and sediment on the spacer placed over the magnetic pattern. Due to gravity, the motion is restricted to a plane parallel to the magnetic pattern. Let $\mathbf{H}_\mathrm{p}(\mathbf{r})$ and $\mathbf{H}_\mathrm{ext}(\hat{\boldsymbol{\omega}})$ be the magnetic field created by the pattern at position $\mathbf{r}$ and by the uniform external magnetic field pointing along $\hat{\boldsymbol{\omega}}$, respectively. The magnitude of the external field is constant and its orientation, $\hat{\boldsymbol{\omega}}(t)$, changes with time t. The total magnetic field is the sum of both contributions

$$\mathbf{H}(\mathbf{r},\hat{\boldsymbol{\omega}}) = \mathbf{H}_\mathrm{p}(\mathbf{r}) + \mathbf{H}_\mathrm{ext}(\hat{\boldsymbol{\omega}}). \tag{S1}$$

Using a point-dipole approximation, the magnetic moment induced on the magnetic particle is $\mathbf{m} = \chi v_\mathrm{p}\mu_0\mathbf{H}$. Here χ is the magnetic susceptibility of the particle, v_p is the particle volume, and μ_0 is the vacuum magnetic permeability.

Within our simple approximation, the potential magnetic energy of the paramagnetic particle in the total magnetic field $\mathbf{H}$ is

$$\begin{aligned} V_\mathrm{m}(\mathbf{r},\hat{\boldsymbol{\omega}}) &= -\chi v_\mathrm{p}\mu_0\mathbf{H}(\mathbf{r},\hat{\boldsymbol{\omega}})\cdot\mathbf{H}(\mathbf{r},\hat{\boldsymbol{\omega}}) \\ &= -\chi v_\mathrm{p}\mu_0\left[\mathbf{H}_\mathrm{p}(\mathbf{r})\cdot\mathbf{H}_\mathrm{p}(\mathbf{r})\right. \\ &\left.+2\mathbf{H}_\mathrm{p}(\mathbf{r})\cdot\mathbf{H}_\mathrm{ext}(\hat{\boldsymbol{\omega}}) + \mathbf{H}_\mathrm{ext}(\hat{\boldsymbol{\omega}})\cdot\mathbf{H}_\mathrm{ext}(\hat{\boldsymbol{\omega}})\right]. \end{aligned} \tag{S2}$$

The external magnetic field is much stronger than that of the pattern. Therefore, we neglect the term $\mathbf{H}_\mathrm{p}^2$ in Eq. (S2), which may also partially account for the quantitative discrepancies between the experimental and the theoretical positions of the fences in $\mathcal{C}$. Furthermore, the term $\mathbf{H}_\mathrm{ext}^2$ in Eq. (S2) is just an irrelevant constant. Hence, to understand the particle transport, we apply the following magnetic potential to the particles

$$V_\mathrm{m}(\mathbf{r},\hat{\boldsymbol{\omega}}) \approx -2\chi v_\mathrm{p}\mu_0\mathbf{H}_\mathrm{p}(\mathbf{r})\cdot\mathbf{H}_\mathrm{ext}(\hat{\boldsymbol{\omega}}). \tag{S3}$$

---

* delasheras.daniel@gmail.com; www.danieldelasheras.com

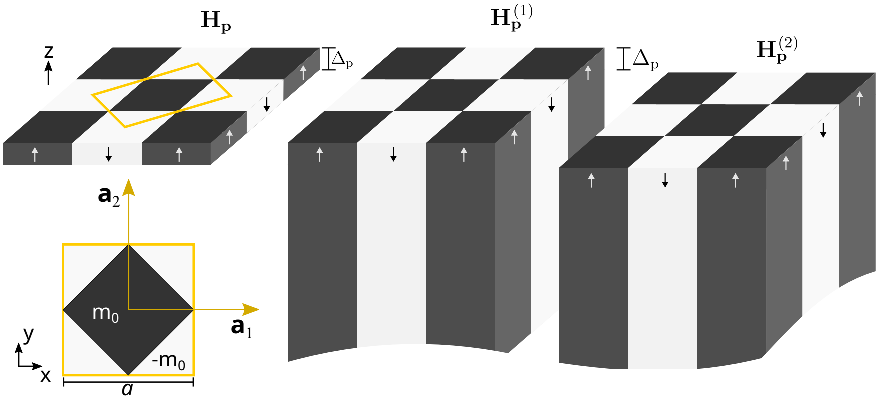

Supplementary Fig. 1. **Magnetic pattern.** The magnetic checkerboard-pattern is a film of thickness Δ_p made of alternating square regions with positive (black) and negative (white) magnetization normal to the pattern (z-direction). The magnetic field $\mathbf{H}_\mathrm{p}$ is calculated as the difference between the fields $\mathbf{H}_\mathrm{p}^{(1)}$ and $\mathbf{H}_\mathrm{p}^{(2)}$, which are those of infinitely thick films displaced by Δ_p in z-direction. A unit cell (yellow square) of the pattern is represented together with the lattice vectors $\mathbf{a}_i$ with $i = 1, 2$ (both of magnitude a) which are parallel to the x- and y-axes as indicated. The saturation magnetization of the domains is m_0.

Within this simplified model, the magnetic force that follows from the negative gradient of the magnetic potential is the only force that acts on the particles. More realistic models [5–7] could include the explicit effect of viscous forces due to the solvent, electrostatic forces, van der Waals forces, friction against the spacer, and gravity. Also, note that the demagnetizing field on the particle will alter the magnitude of the effective magnetization [8] and that the point-dipole approximation will not be accurate enough sufficiently close to the pattern since the pattern field will vary significantly across the particle volume. To obtain a rough estimate of the accuracy of the point-dipole approximation, we computed an effective pattern field by averaging $\mathbf{H}_\mathrm{p}$ over the particle volume:

$$\mathbf{H}_\mathrm{p}^\mathrm{eff}(\mathbf{r}) = \frac{1}{v_\mathrm{p}} \int d\mathbf{r}' \Theta(\mathbf{r}' - d_0/2) \mathbf{H}_\mathrm{p}(\mathbf{r} - \mathbf{r}'), \tag{S4}$$

where $\Theta(\cdot)$ is the Heaviside step function and d_0 the diameter of the particle. We then verified that the gradients of the effective field, $\nabla \mathbf{H}_\mathrm{p}^\mathrm{eff}(\mathbf{r})$, differ by less than one percent from those of the original field, $\nabla \mathbf{H}_\mathrm{p}(\mathbf{r})$. Also, the term $\mathbf{H}_\mathrm{p}^2$ in Eq. (S2) can play a relevant role at low enough elevations. Despite the simplicity of the model, we obtain a good qualitative comparison with the experiments due to the motion being topologically protected.

C. Equation of motion

The colloidal particles move around an equilibrium elevation above the pattern, with their center of mass approximately confined to a plane parallel to the pattern. The position vector of a particle of radius $d_0/2$, which has sedimented onto the coating layer of the pattern (effective thickness Δ), is given by $\mathbf{r}_\mathrm{c} = (x, y, d_0/2 + \Delta)$. Neither inertia nor Brownian motion play a significant role in the experiments, as the magnetic forces strongly dominate the particle transport. Therefore, we simulate the system using the overdamped Brownian dynamics equation of motion in the limit of negligible thermal fluctuations. That is, the position of the particle is given by

$$\gamma \dot{\mathbf{r}}_\mathrm{c} = -\nabla_\mathcal{A} V_\mathrm{m}(\mathbf{r}_\mathrm{c}, \hat{\boldsymbol{\omega}}), \tag{S5}$$

where γ is the friction coefficient against the implicit solvent (we assume that there is no friction between the particles and the spacer), the overdot indicates time derivative, and $\nabla_\mathcal{A} = (\nabla_x, \nabla_y, 0)$ with $\nabla_\alpha = \frac{\partial}{\partial \alpha}$ and $\alpha = \{x, y\}$. Note that no particle motion occurs in z-direction and that there are no interactions between the colloidal particles because the system is very dilute. We solve numerically the above equation of motion to find the particle trajectories.

D. Magnetic field of the pattern

The pattern is a thin film of alternating domains with positive and negative magnetization, see supplementary Fig. 1. Let $\mathbf{H}_\mathrm{p}^{(1)}$ and $\mathbf{H}_\mathrm{p}^{(2)}$ be the magnetic fields generated by two identical and infinitely thick checkerboard patterns with their pattern-air interfaces being defined by the planes $z_1 = 0$ and $z_2 = -\Delta_\mathrm{p}$, respectively (see schematic in supplementary Fig. 1). Then, the magnetic film of a thin pattern of thickness Δ_p can be calculated as

$$\mathbf{H}_\mathrm{p}(\mathbf{r}) = \mathbf{H}_\mathrm{p}^{(1)}(\mathbf{r}) - \mathbf{H}_\mathrm{p}^{(2)}(\mathbf{r}). \tag{S6}$$

Given that there are no free currents, we calculate the magnetic fields of the thick patterns via the magnetic scalar potentials $\psi^{(i)}(\mathbf{r})$ with $i = 1, 2$. That is,

$$\mathbf{H}_\mathrm{p}^{(i)}(\mathbf{r}) = -\nabla \psi^{(i)}(\mathbf{r}), \tag{S7}$$

where ∇ denotes the gradient with respect to $\mathbf{r}$. The magnetic scalar potential satisfies the Laplace equation

$$\nabla^2\psi^{(i)}(\mathbf{r}) = 0. \tag{S8}$$

The magnetization is normal to the patterns (along the z-axis). Hence, the boundary conditions for the magnetic field of the thick patterns read

$$\mathbf{H}_\mathrm{p}^{(i)}(\mathbf{r})\Big|_{z_i}\cdot\hat{\mathbf{e}}_z = \mathbf{M}_\mathrm{p}^{(i)}(\mathbf{r})\Big|_{z_i}\cdot\hat{\mathbf{e}}_z, \tag{S9}$$

where $\hat{\mathbf{e}}_z$ is the unit vector along the z-axis (normal to the pattern), z_i is the position of the air-pattern interface of the i-thick pattern, and $\mathbf{M}_\mathrm{p}^{(i)}$ is its magnetization given by

$$\mathbf{M}_\mathrm{p}^{(i)}(\mathbf{r}) = M_\mathrm{sq}(\mathbf{r}_\perp)\Theta(z_i - z)\hat{\mathbf{e}}_z, \tag{S10}$$

with $\mathbf{r}_\perp = (x, y)$, and

$$M_\mathrm{sq}(\mathbf{r}_\perp) = m_0\mathrm{sign}\left(\sum_{j=1}^{2}\cos(\boldsymbol{q}_j\cdot\mathbf{r}_\perp)\right), \tag{S11}$$

where m_0 is the saturation magnetization of the domains. The wave vectors q_j, with magnitude $q_0 = 2\pi/a$, are the reciprocal vectors of the lattice vectors. That is, $\boldsymbol{a}_i\cdot\boldsymbol{q}_j = 2\pi\delta_{ij}$ with δ_{ij} being the Kronecker delta.

We calculate the magnetic field of the thick patterns with two different methods that yield the same results within the expected numerical precision. In the first method, we find $\mathbf{H}_\mathrm{p}^{(i)}$ via Eq. (S7) by solving with Fourier series the Laplace equation for the magnetostatic potential (S8) subject to the boundary condition (S9) and using that $\mathbf{H}_\mathrm{p}^{(i)}$ decays to zero far apart from the pattern, i.e., $\lim_{z\to\infty}\mathbf{H}_\mathrm{p}^{(i)}(\mathbf{r}) = 0$. For the second method, we calculate $\mathbf{H}_\mathrm{p}^{(i)}$ using the Green's function of the Laplace operator which yields

$$\mathbf{H}_\mathrm{p}^{(i)}(\mathbf{r}) = \nabla\int d\mathbf{r}'\frac{\nabla'\cdot\mathbf{M}_\mathrm{p}^{(i)}(\mathbf{r}')}{4\pi|\mathbf{r}-\mathbf{r}'|}, \tag{S12}$$

with ∇' indicating derivative with respect to $\mathbf{r}'$. Using Eq. (S10) for the magnetization of an infinitely thick checkerboard pattern gives

$$\mathbf{H}_\mathrm{p}^{(i)}(\mathbf{r}) = \int d\mathbf{r}'_\perp\frac{\mathbf{r}_\perp - \mathbf{r}'_\perp + (z - z_i)\hat{\mathbf{e}}_z}{4\pi|\mathbf{r}_\perp - \mathbf{r}'_\perp + (z - z_i)\hat{\mathbf{e}}_z|^3}M_\mathrm{sq}(\mathbf{r}'_\perp). \tag{S13}$$

We calculate the space integral in the above equation numerically.

E. Fences of patterns with blurred magnetic interfaces.

The angular width of the diamond-shaped fences as a function of elevation is shown in Supplementary Fig. 2.

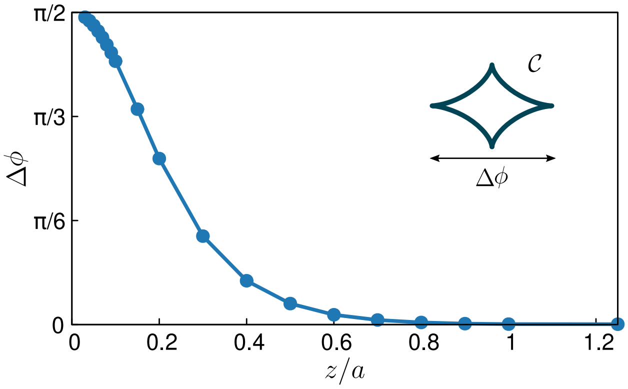

Supplementary Fig. 2. **Fence size.** Size of the diamond-shaped fences in control space, $\Delta\phi$, as a function of the height above the pattern scaled with the length of a lattice vector, z/a. The fence size is expressed in radians and it is defined as the maximum angular width of the fence in the azimuthal direction ϕ (see the schematic inset which depicts a fence in control space).

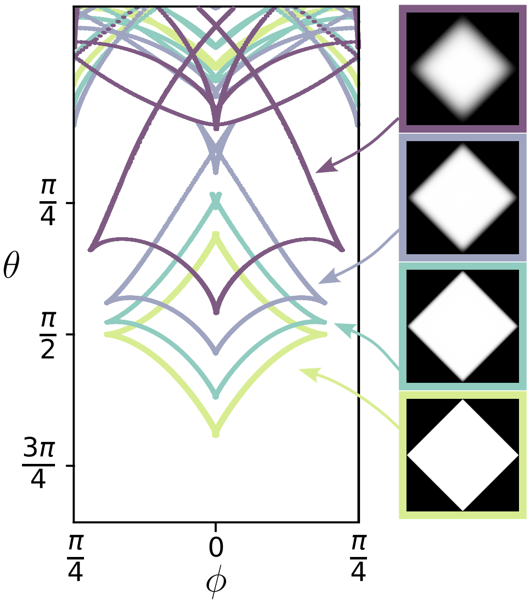

Supplementary Fig. 3. **Effect of blurred interfaces.** A region of control space (Mercator projection) depicting one fence of checkerboard-patterns with blurred edges between regions of opposite magnetization. In all cases the fences are calculated at a distance $z/a = 0.125$ above the pattern.

The position and the shape of the fences in $\mathcal{C}$ do not exactly coincide between experiments and simulations. See, for example, the differences between the experimental driving loop and that used in simulations in Fig. 3 of the main paper. Our goal is not to predict the exact position and shape of the fences, but rather to understand the topology of control space. Knowledge of the topological properties of $\mathcal{C}$ makes it is simple to design and adjust loops that induce transport in the experiments.

Nevertheless, understanding the possible origin of

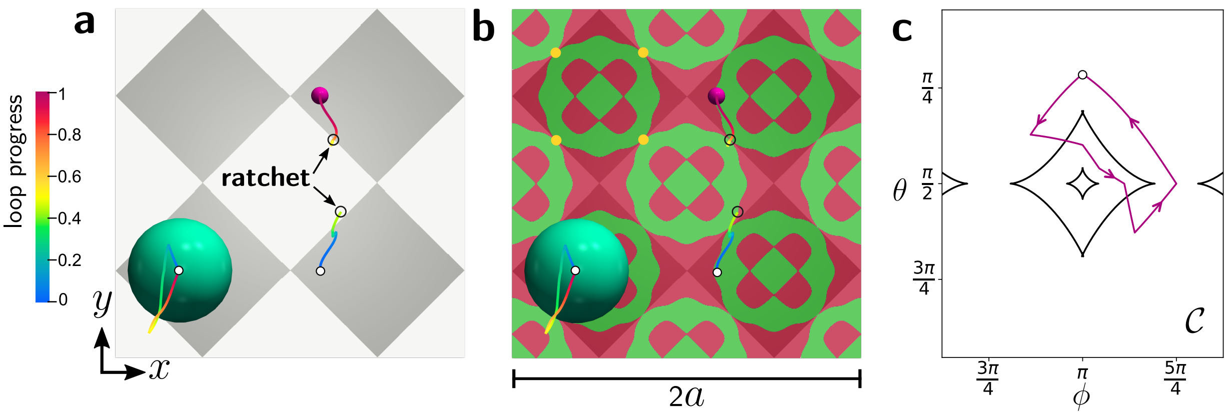

Supplementary Fig. 4. **Ratchet motion.** Magnetization (a) and action space (b) with allowed (green) and forbidden regions (red). A large particle (green) and a small particle (violet) moving at elevations $0.375a$ and $0.125a$, respectively, are shown. (c) Control space (mapped in Mercator projection) showing the fences (black solid lines) and a modulation loop (violet solid line) winding counterclockwise and inducing a ratchet motion for the small particle. The white circles denote the starting point of trajectories in (a,b) and that of the loop in (c). The trajectories are coloured according to the loop progress (see colour bar). Four gates in (b) are indicated with yellow circles. The small particle (violet) performs a ratchet motion and moves one unit cell after completion of the modulation loop. The starting and ending points of the ratchet jump are indicated with empty circles in (a,b) and coincide with the location of the fences in $\mathcal{A}$. The large particle (green) performs a closed trajectory.

these differences is valuable. Local defects or variations in both the polymer coating and the magnetic pattern are to be expected and might affect the fences at specific locations. Polydispersity in particle size will also lead to variations in the positions of the fences between particles belonging to the same species. Moreover, global differences in the position and shape of the fences may arise for several reasons, including discrepancies between the experimental and theoretical distances to the magnetic pattern, uncertainties in the relative orientation between the external field and the pattern, and spatial non-uniformities of the external magnetic field. In addition, in the experiments the saturation magnetization of the pattern might be slightly different in up- and down-magnetized regions and the interfaces between two magnetic domains are not perfectly sharp.

We have calculated how the fences in $\mathcal{C}$ change when the edges between magnetic domains are blurred and one type of magnetic domain becomes more prominent, see supplementary Fig. 3. To blur the edges, we apply a Gaussian filter to the white regions, which results in normal magnetization of variable strength. Under these conditions, the fences systematically shift toward one pole of control space, accompanied by an overall enlargement and deformation of their shape. We believe that this effect is one of the main contributors to the discrepancies observed between the experimental and theoretical fence positions.

F. Ratchet vs adiabatic transport

In the high-elevation limit, the fences in $\mathcal{C}$ reduce to points, and the colloidal transport is adiabatic, meaning that particles are transported exclusively via minima of the magnetic potential. At finite elevations, however, the fences in $\mathcal{C}$ are no longer points but closed curves. In certain cases, a minimum of the potential can be annihilated with a saddle point when the modulation loop crosses a fence in $\mathcal{C}$ from the convex to the concave side. If such minimum is occupied by a particle, then its motion is no longer adiabatic. Instead, the particle undergoes a ratchet-like motion until it reaches a new minimum of the potential. An example of a loop in $\mathcal{C}$ inducing a ratchet together with the corresponding particle trajectory in $\mathcal{A}$ is shown in supplementary Fig. 4. As in previous examples, the loop crosses two gates (gates g_4 and g_3 in Fig. 4d of the main text) but it winds around one fence segment only. The loop induces a ratchet for particles within a given size interval. If the particle is too small or too large, such a loop would not wind around the corresponding fence segments and would not induce transport. Hence, by varying the angular size of the loop in $\mathcal{C}$ as a function of time, we can sequentially activate the motion of a collection of particles from the smallest to the largest particle. An illustrative video is provided with the supplemental material.

---

[1] C. Chappert, H. Bernas, J. Ferré, V. Kottler, J.-P. Jamet, Y. Chen, E. Cambril, T. Devolder, F. Rousseaux, V. Mathet, and H. Launois, Planar patterned magnetic media obtained by ion irradiation, Science **280**, 1919 (1998).

[2] M. Urbaniak, P. Kuświk, Z. Kurant, M. Tekielak, D. Engel, D. Lengemann, B. Szymański, M. Schmidt, J. Alek-

siejew, A. Maziewski, A. Ehresmann, and F. Stobiecki, Domain-wall movement control in Co/Au multilayers by He^+-ion-bombardment-induced lateral coercivity gradients, Phys. Rev. Lett. **105**, 067202 (2010).

[3] P. Kuświk, A. Ehresmann, M. Tekielak, B. Szymański, I. Sveklo, P. Mazalski, D. Engel, J. Kisielewski, D. Lengemann, M. Urbaniak, C. Schmidt, A. Maziewski, and F. Stobiecki, Colloidal domain lithography for regularly arranged artificial magnetic out-of-plane monodomains in Au/Co/Au layers, Nanotechnol. **22**, 095302 (2011).

[4] J. Loehr, D. de las Heras, M. Loenne, J. Bugase, A. Jarosz, M. Urbaniak, F. Stobiecki, A. Tomita, R. Huhnstock, I. Koch, A. Ehresmann, D. Holzinger, and T. M. Fischer, Lattice symmetries and the topologically protected transport of colloidal particles, Soft Matter **13**, 5044 (2017).

[5] M. Urbaniak, D. Holzinger, A. Ehresmann, and F. Stobiecki, Magnetophoretic lensing by concentric topographic cylinders of perpendicular magnetic anisotropy multilayers, Biomicrofluidics **12**, 044117 (2018).

[6] F. Klingbeil, F. Block, U. Sajjad, R. B. Holländer, S. Deshpande, and J. McCord, Evaluating and forecasting movement patterns of magnetically driven microbeads in complex geometries, Sci. Rep. **10**, 8761 (2020).

[7] M. Urbaniak, D. Kiphart, M. Matczak, F. Stobiecki, G. D. Chaves-O'Flynn, and P. Kuświk, Ferrimagnetic Tb/Co multilayers patterned by ion bombardment as substrates for magnetophoresis, Sci. Rep. **14**, 23771 (2024).

[8] B. Yellen, G. Friedman, and A. Feinerman, Analysis of interactions for magnetic particles assembling on magnetic templates, J. Appl. Phys. **91**, 8552 (2002).